Structural Characterization of Advanced Composite Tow-Steered Shells with Large Cutouts

K. Chauncey Wu[1] and Jason D. Turpin[2]
NASA Langley Research Center, Hampton, VA 23681

Nathaniel W. Gardner[3]
Analytical Services and Materials, Inc., Hampton, VA 23666

Bret K. Stanford[4] and Robert A. Martin[5]
NASA Langley Research Center, Hampton, VA 23681

The structural performance of two advanced composite tow-steered shells with large cutouts, manufactured using an automated fiber placement system, is assessed using both experimental and analytical methods. The fiber orientation angles of the shells vary continuously around their circumference from ±10 degrees on the crown and keel, to ±45 degrees on the sides. The raised surface features on one shell result from application of all 24 tows during each fiber placement system pass, while the second shell uses the tow drop/add capability of the system to achieve a more uniform wall thickness. These unstiffened shells, both without and with small cutouts, were previously tested in axial compression and buckled elastically. In this study, a single unreinforced cutout, scaled to represent a cargo door on a commercial aircraft, is machined into one side of each shell. The prebuckling axial stiffnesses and bifurcation buckling loads of these shells with large cutouts are also computed using linear finite element structural analyses for preliminary comparisons with test data. During testing, large displacements are observed around the large cutouts, but the shells maintain an average of 91 percent of the axial stiffness, and also carry 85 percent of the buckling loads, when compared to the pristine shells without cutouts. These relatively small reductions indicate that there is great potential for using tow steering to mitigate the adverse effects of large cutouts on the overall structural performance.

I. Introduction

CUTOUTS in aerospace structures range in size from very large, as shown in Fig. 1, to very small, and provide access for loading or unloading passengers or cargo, maintenance and inspection, or windows or vents. However, these cutouts also result in structural load path discontinuities, with associated losses in structural performance.[1, 2] These losses in overall stiffness and strength are typically mitigated by substantial reinforcement of the structure surrounding the cutout.[2] However, a more efficient solution for structures built from laminated fibrous composites may take advantage of the highly directional nature of composites to redirect the global applied loads either around, or away from, the cutout,[3, 4] with the goal of minimizing the additional reinforcements and associated weight penalty required around that discontinuity.

Traditionally, strength and stiffness tailoring of conventional composite laminates is achieved by deploying integer numbers of unidirectional plies that are oriented at one of a limited subset (typically 0, ±45, and 90 degrees) of the wider range of possible fiber orientation angles. When this fiber orientation angle is instead allowed to vary continuously over the structural planform within each lamina, these tow-steered designs are designated as advanced

---

[1] Senior Research Engineer, Structural Mechanics and Concepts Branch, Research Directorate, Mail Stop 190. AIAA Member

[2] LARSS student assigned to the Structural Mechanics and Concepts Branch, Research Directorate. Sponsored by the Kansas Space Grant Consortium, Wichita, KS 67260. Presently employed at Spirit AeroSystems Inc., Wichita, KS 67278. AIAA Member

[3] Senior Scientist, supporting the Structural Mechanics and Concepts Branch, Research Directorate, Mail Stop 190

[4] Research Engineer, Aeroelasticity Branch, Research Directorate, Mail Stop 340. AIAA Member

[5] Senior Aerospace Engineer, Mechanical Systems Branch, Engineering Directorate, Mail Stop 432

composite structures[5] to better differentiate them from the conventional straight-fiber laminates. These tow-steered composites are readily fabricated using automated fiber placement systems,[6, 7] such as the one shown in Fig. 2, that are now widely used in the aerospace industry for fabrication of primary structures. These large computer-numerically-controlled machine tools can place a large number of continuous, unidirectional prepreg composite tows or slit-tape material, each up to 1/2 in.-wide, onto a mandrel or tool surface, while also precisely and accurately following predefined curvilinear spatial paths.

Figure 1. Aircraft with large cutout.

Figure 2. Automated fiber placement system.

Since advanced composite tow-steered structures have not been widely deployed in operational service, they have not been studied as extensively as more conventional straight-fiber composites. In addition, the techniques required for their structural design, modeling, analyses and certification are not currently as well defined or understood as they are for more conventional composites. To help expand the database of knowledge and practical experience with advanced composite structures, two prototype tow-steered composite shells were designed,[8] manufactured, and then surveyed to determine their geometric imperfections and wall thicknesses.[9]

Experimental studies and preliminary finite element analyses of these pristine (i.e., without cutouts) shells were performed to evaluate their structural response under axial compression loads.[10] The observed linear prebuckling, global buckling and nonlinear postbuckling behaviors for both shells were characterized as elastic, with no visible

indications of material damage after testing. This assessment was verified by repeating the compression test for one of the shells, with minimal differences noted between tests in both the measured prebuckling axial stiffness and global buckling load. To take advantage of this elastic recovery, the same test articles were then modified to include unreinforced, scaled passenger door-size cutouts and retested.[11] The cutouts for the shells assessed in Ref. 11 are hereafter designated as "small" cutouts to better differentiate them from the larger cutouts evaluated in this study.

In the present study, compression tests of these tow-steered composite shells with large cutouts were performed to assess their structural behavior under displacement-controlled end loading. The resulting axial stiffness, buckling, and postbuckling behaviors of these shells were measured, characterized, and compared with selected corresponding results for the same shells previously tested without cutouts and with small cutouts.

II. Tow-steered shell description

Both of the unstiffened shells evaluated in this study had fiber orientation angles that vary continuously around the cylinder circumference. These shells were originally designed without cutouts, and to have different cross-sectional bending stiffnesses about their transverse axes.[8] The fiber orientation angle Θ on both shells was steered to vary continuously from ±10 degrees on the shell crown and keel, to ±45 degrees on the shell sides along a constant-radius circular arc, as shown in Fig. 3. One possible application for this type of structure could be an advanced commercial aircraft fuselage, which may be assumed to behave like a beam in bending under applied flight loads. In this application, the fuselage crown and keel experience longitudinal compression and tension loads, and the shell sides are subjected to shear as the loads transfer between the crown and keel.

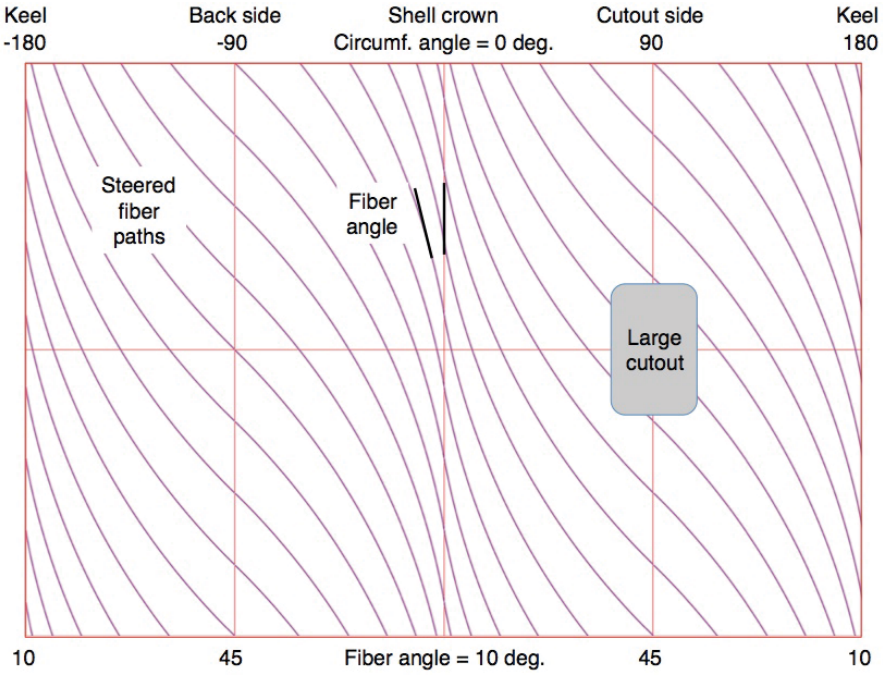

Figure 3. Planform view of tow-steered shell with large cutout.

These cylindrical shells were fabricated using the automated fiber placement system shown in Fig. 2.[9] The nominal eight-ply laminate thickness was approximately 0.040 in., with a nominal inner diameter for both shells of 16.266 in. and a 35.0-in. overall length. The shells were manufactured using 1/8 in.-wide IM7/8552 graphite/epoxy slit tape material oriented in a nominal $[\pm 45/\pm\Theta]_S$ layup, where Θ is the steered fiber orientation angle. The material properties used for the finite element analyses were developed in Refs. 10 and 11.

During fabrication, a maximum of 24 tows were placed by the fiber placement system at each location on the shell planform. When all 24 tows were placed during each pass of the fiber placement system (also called a course), a regular pattern of thicker tow overlaps (up to 16 plies, or 0.080 in. thickness) was generated between adjacent courses on the shell crown and keel regions.[8-11] However, these courses were defined and spaced so that they did not overlap along the shell sides. These resulting laminate thickness build-ups led to designation of this test specimen as the shell with overlaps, also designated as Shell A in Refs. 10 and 11. For the second test specimen, individual tows

were cut (or "dropped") or added at various points during its fabrication, resulting in a more uniform laminate thickness[9] and subsequent designation as the shell without overlaps, also called Shell B in Refs. 10 and 11. These two configurations represent practical bounds on the weights and fabrication of the shells.

After compression tests were completed on both the pristine shells[10] and shells with small cutouts,[11] flash thermography[12] was performed to identify any potential internal damage caused during these tests. No obvious damage to either shell was noted during these assessments. Following non-destructive examination, a single large cutout, completely surrounding the smaller cutouts, was then machined into the center of one side of each shell where the nominal wall layup is $[(\pm 45)_2]_S$, as shown in Fig. 3.

These unreinforced large cutouts shown in Fig. 4 were scaled and oriented to represent a cargo door on a commercial aircraft.[13] The cutouts measured 8 in. along the shell longitudinal dimension by 5-1/4 in. (approximately one-third of the nominal shell diameter) in the circumferential dimension, with 3/4-in. corner radii. The shells were then prepared for testing by installing 48 additional strain gages in back-to-back pairs of axial, biaxial, and triaxial rosettes around the cutout perimeter, also shown in Fig. 4. After the strain gages were installed, the region around the cutouts was repainted with a black base coat and speckled for measurements gathered during testing using three-dimensional digital image correlation (DIC) systems.[14]

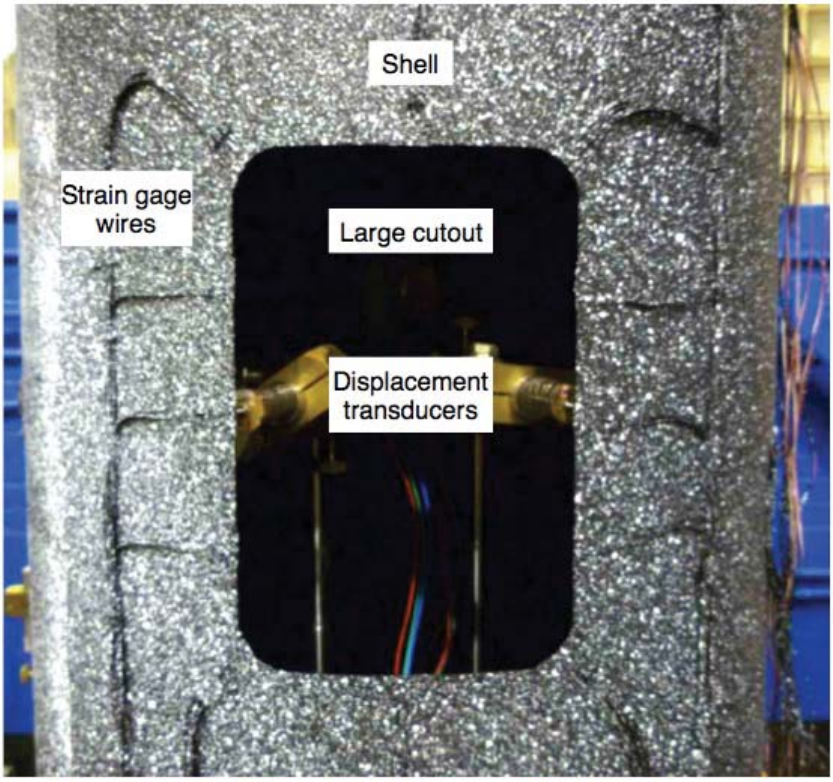

Figure 4. Detail of large cutout and test instrumentation.

III. Shell compression test set-up

Compression tests of the pristine tow-steered shells without cutouts were performed to evaluate their structural performance.[10] In those baseline tests, Shell A, the shell with overlaps, exhibited a linear prebuckling axial stiffness of 531.2 klb/in., and buckled at 38.8 klbs. In comparison, Shell B, the shell without overlaps, had a prebuckling stiffness of 328.7 klb/in., and buckled at 17.2 klbs. The shells were loaded into deep postbuckling to approximately two times the end shortening observed at global buckling, but they did not experience material failure in these initial tests. Both shells responded elastically throughout the applied loading, with no visible indications of damage on the composite laminates after the baseline tests were completed.

To gain more knowledge and insight into the behavior of these structures, a small cutout with dimensions of 3 in. by 4-7/8 in. along the shell longitudinal and circumferential axes, respectively, was then cut into the center of one side of each shell. When the compression tests were performed again,[11] Shell A, the shell with overlaps,

exhibited a linear prebuckling axial stiffness of 497.1 klb/in., and buckled at 31.8 klbs. Shell B, the shell without overlaps, had a prebuckling stiffness of 299.5 klb/in., with global buckling at 15.5 klbs. After these shells buckled and achieved a stable postbuckled state, they were then unloaded back to zero load. Both shells again responded elastically, and appeared undamaged after the tests were concluded.

The same test setup and hardware shown in Fig. 5 were used for the present tests on the shells with large cutouts. For these tests, a DIC system was positioned to view the structural response of the shell side containing the large cutout. The stiffer shell crown and keel were oriented along the left-right axis of the test stand, and a second DIC system was mounted to assess the structural response of the shell crown on the left side of the test stand. Note that designation of the shell crown and keel is arbitrary because of its symmetry with respect to its side-to-side axis.

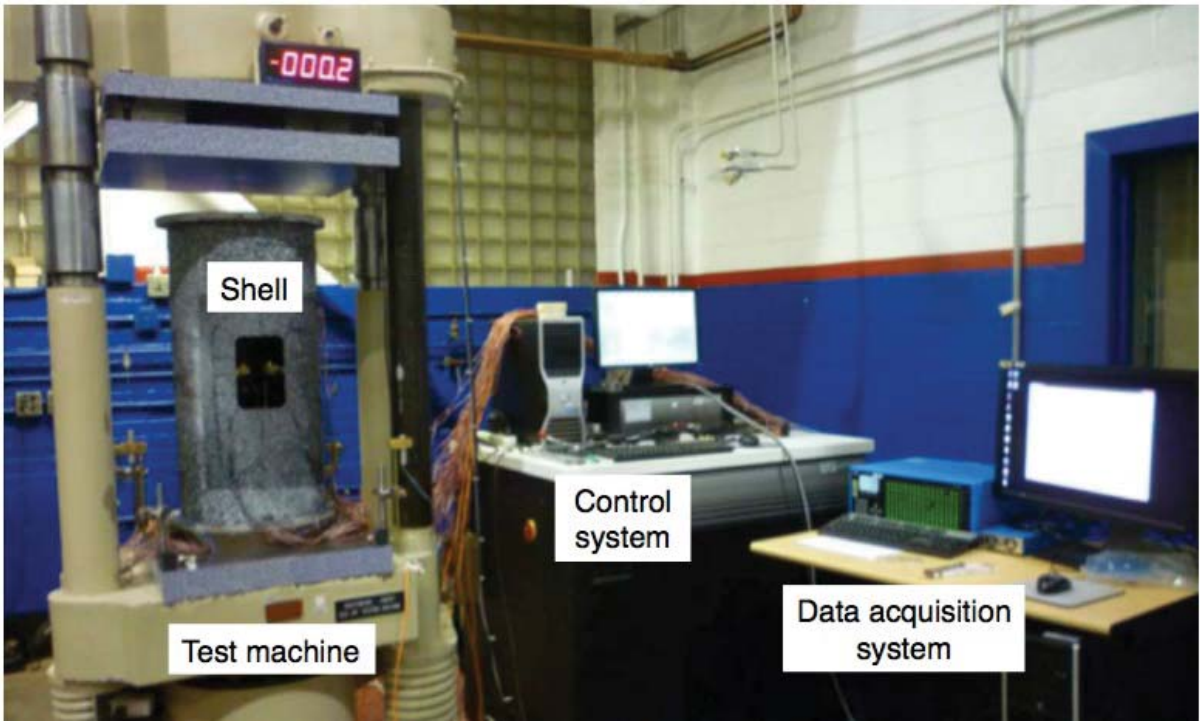

Figure 5. Tow-steered shell with large cutout in test stand.

IV. Shell compression test results

The resulting axial stiffness, buckling, and postbuckling behaviors of the shells with large cutouts are presented and discussed in this section. These results are directly comparable with the results presented in Refs. 10 and 11 because the same test articles and methodologies are used, with the only difference being the increased size of the cutouts in the present test articles. The validity of these results os also predicated on the assumption that the previous tests did not caused invisible damage to the shells, an assumption that was verified using thermographic non-destructive inspection and evaluation.

A. End shortening, axial stiffness and buckling

Displacement transducers were located at each of the four corners of the test stand to measure the relative motion of the platens while the shell was loaded in end compression. These individual measurements were averaged, and the results plotted against the axial load in Figs. 6 and 7 for Shells A and B, respectively. As discussed in Refs. 10 and 11, the load-end shortening response for these shells may be separated into several distinct regions, (1) linear prebuckling, (2) buckling (occurring in a matter of milliseconds) and stable postbuckling, (3) nonlinear elastic unloading, and (4) linear elastic unloading, as indicated in Figs. 6 and 7.

The shell prebuckling axial stiffness was calculated from a least-squares best fit slope to the linear portion of the prebuckling load-end shortening curve. The measured axial stiffnesses for the shells with large cutouts, listed in Table 1, are 488.6 klb/in. for Shell A, and 295.6 klb/in. for Shell B. This measured axial stiffness of Shell A with a large cutout is 65 percent higher than that of Shell B with a large cutout, as compared to 62 percent in the baseline tests in Ref. 10. In addition, these axial stiffnesses for Shells A and B with large cutouts are 92 and 90 percent,

respectively, of the corresponding values for the same shells without cutouts, for an average stiffness reduction of 9 percent.

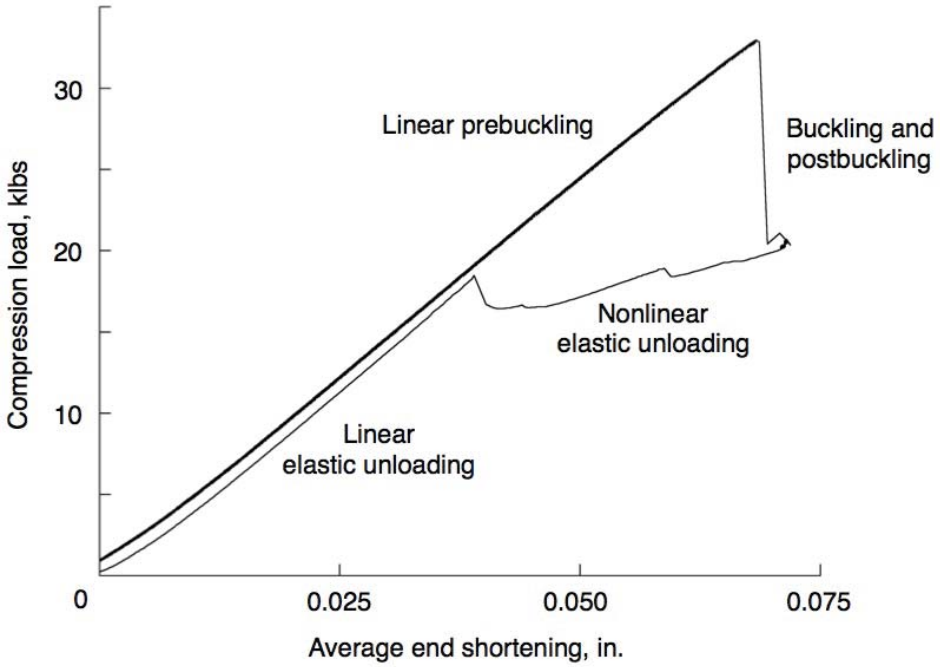

Figure 6. Shell A axial load plotted as a function of end shortening.

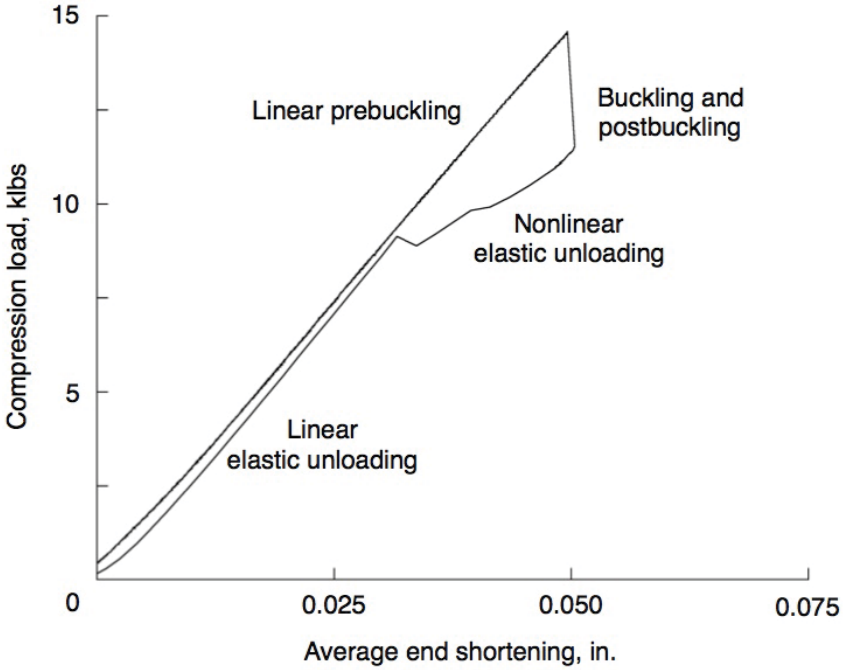

Figure 7. Shell B axial load plotted as a function of end shortening.

At the peak load, Shells A and B failed in global buckling at 33.0 klbs and 14.6 klbs axial load, respectively, as noted in Table 1. The buckling load for Shell A with a large cutout is 105 percent higher than that of Shell B with a large cutout, whereas the corresponding value was 126 percent from the baseline tests. The buckling loads for the shells with large cutouts are both equal to 85 percent of the buckling load for the same shells tested in their pristine configurations.

Immediately following global buckling, the axial load dropped rapidly to 20.4 klbs and 11.5 klbs for Shells A and B, respectively. These stable postbuckling loads are also listed in Table 1. Shell B with the large cutout has a postbuckling load that is 9 percent lower than the measured postbuckling load of 12.6 klbs for the same shell without a cutout. However, Shell A with the same cutout carries a postbuckling load of 20.4 klbs, which is 18 percent greater than the 17.3 klb postbuckling load for that shell without a cutout. Since intuition might suggest that the postbuckling load should be lower for a shell with a cutout, this result seems counterintuitive, and may warrant further investigation with nonlinear structural analyses.

Table 1. Measured performance for shells with large cutouts

Shell performance metric	Shell A	Shell B
Prebuckling axial stiffness, klb/in.	488.6	295.6
Global buckling load, klbs	33.0	14.6
Postbuckling load, klbs	20.4	11.5

B. Prebuckling acreage strains

Laminate surface strains were measured during the shell compression tests using a total of 110 strain gages mounted in back-to-back pairs to the shell inner and outer surfaces. These gages, installed in longitudinal, circumferential, and shear orientations, provided data on the shell structural response at discrete locations across the shell planform. The majority of these gages were deployed across the shell acreage near the crown, keel, and sides, as shown in Fig. 8. In this section, selected acreage strains are plotted against the measured axial load up to shell buckling, and the results from compression tests on both shells are discussed in more detail.

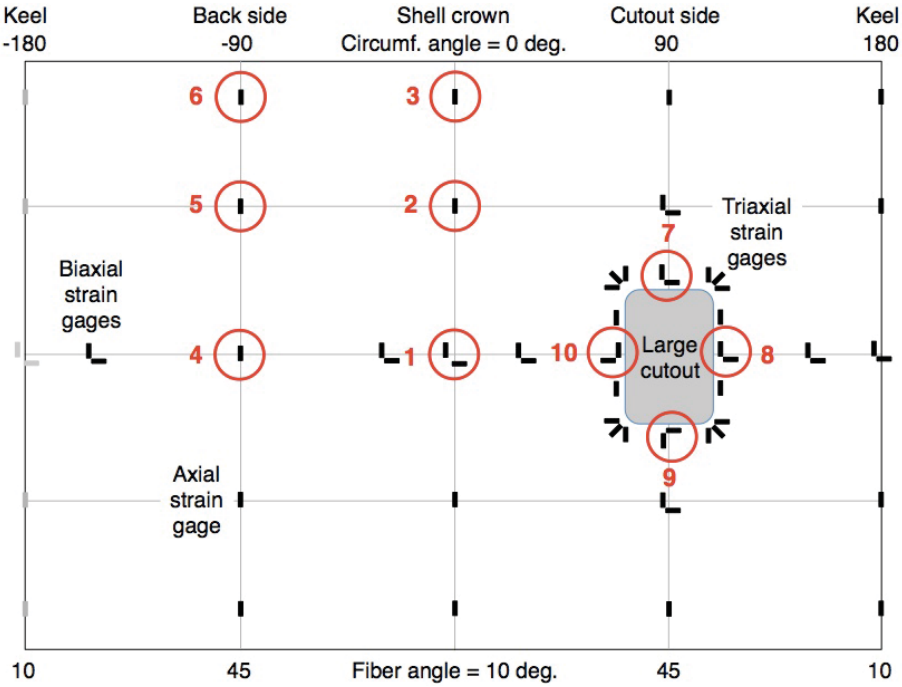

Figure 8. Strain gage rosette locations (shell exterior planform shown).

The measured axial strains at several locations along the crown of Shells A and B are plotted against the axial load in Figs. 9 and 10, respectively. The back-to-back strain gages were located at the shell mid-length, at 75 percent of the shell length, and adjacent to the upper potted end. These rosette locations (abbreviated as RL) are denoted as RL 1, 2, and 3, respectively, in Fig. 8. The plotted strains for both shells increase in proportion to the load and, except at RL 1, diverge monotonically with increasing load. However, the plotted strains for both shells at RL 1 diverge slightly with increasing load, and then converge rapidly as the load approached buckling. These trends are consistent with the measured strains in both shells along the lower half of the crown and the keel, and reflect the biaxial symmetry of the shell geometry and layup.

The difference between axial strains on the outside and inside of the shell at the same gage location is a quantitative measure of the local transverse bending. Much higher bending is observed along the shell crown towards the potted ends than towards the mid-length, which is characteristic of the bending boundary layer that is generated near the ends of compression-loaded shells. As noted previously, the strains at RL 1 tend to converge just before global buckling. This convergent behavior indicates that the magnitude of the bending moment at that location decreased with increasing load.

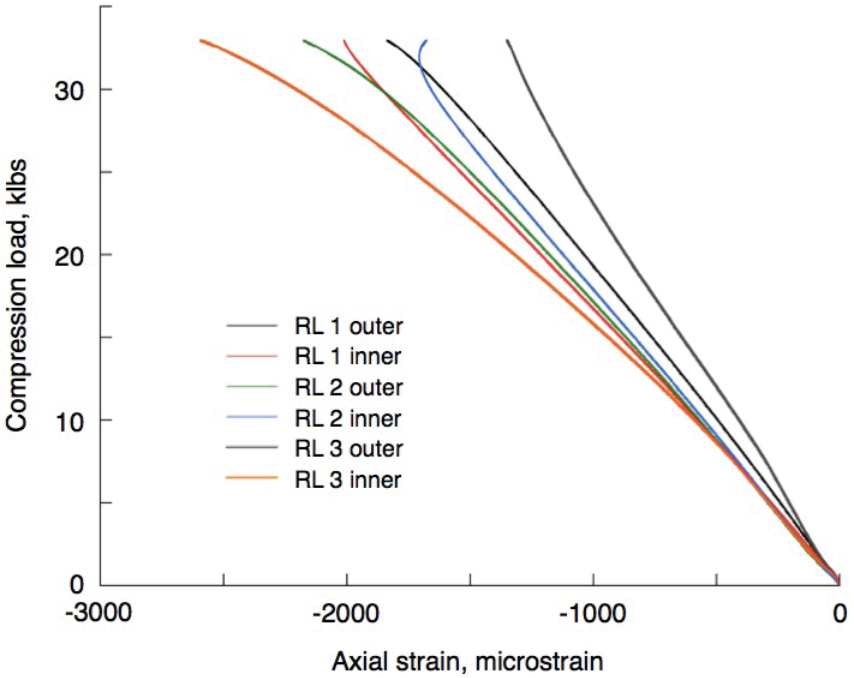

Figure 9. Shell A axial load plotted as a function of crown axial strain.

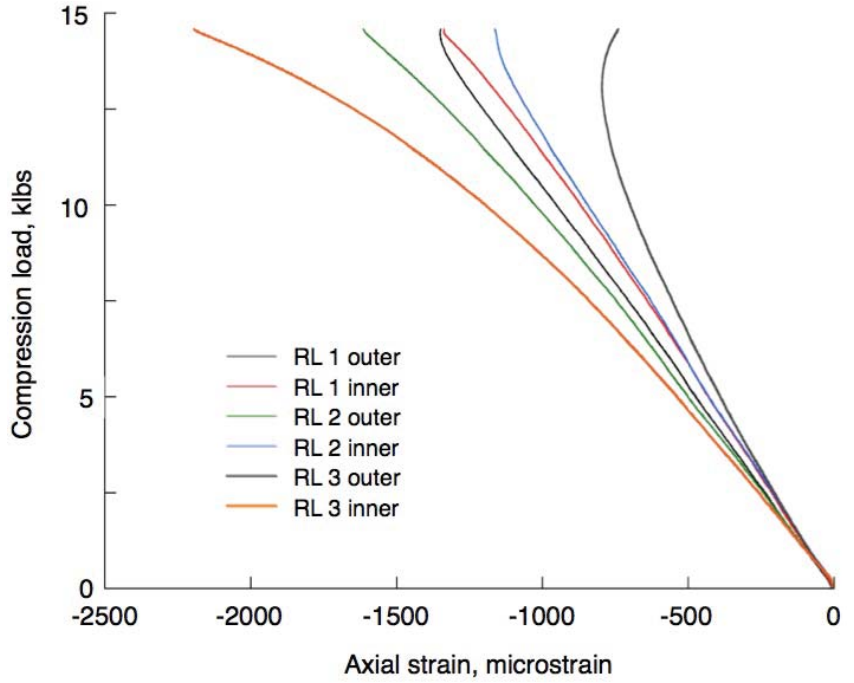

Figure 10. Shell B axial load plotted as a function of crown axial strain.

Measured axial strain responses from gages on the back sides of the shells diametrically opposite from the cutouts are plotted in Fig. 11 for Shell A, and Fig. 12 for Shell B. These gage locations are designated as RL 4, 5, and 6 in Fig. 8, and are located at the same positions along the shell length as reported above for the strains on the shell crown. The back-side strains for both shells are much more linear than the corresponding strains in Figs. 9 and 10. In addition, the strain traces at RL 4 and 5 on both shells agree very well, meaning that very little bending is occurring near the middle of the shells along the sides. For both shells, the strain traces at RL 6 deviate with increasing load, which indicates that more bending takes place near the potted shell ends than towards the shell mid-length. This observation suggests that there is also a bending boundary layer located near the potted ends along the shell sides, and is consistent with the same observation made for the shell crowns.

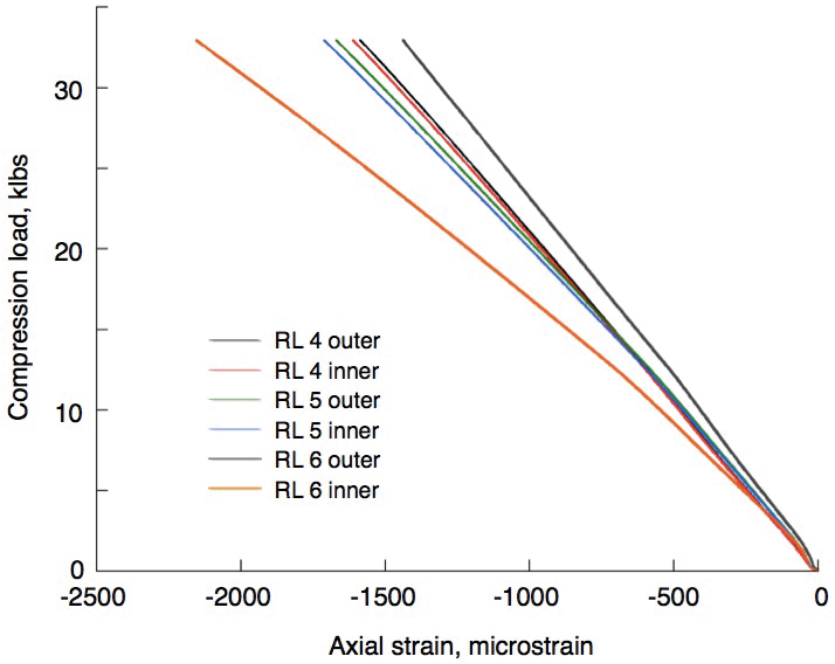

Figure 11. Shell A axial load plotted as a function of back side axial strain.

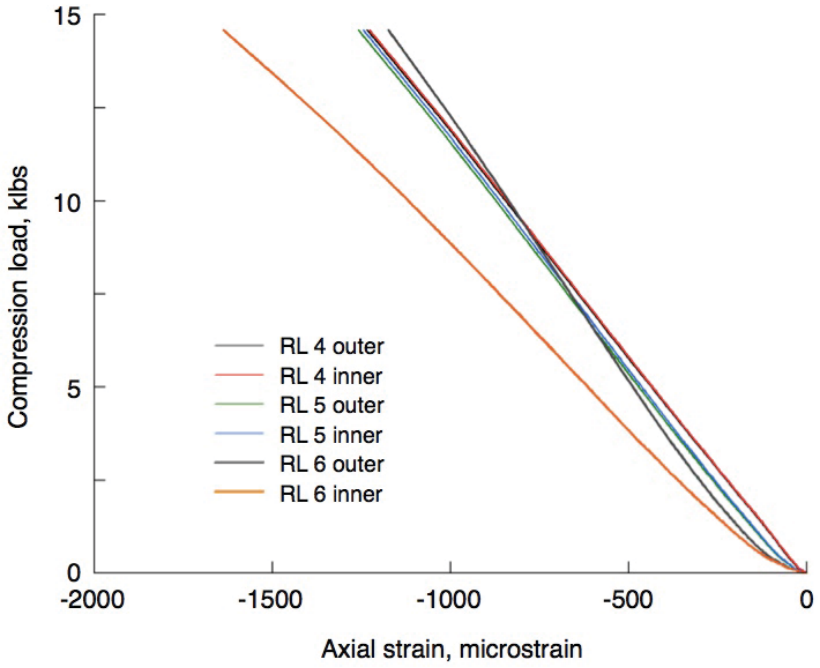

Figure 12. Shell B axial load plotted as a function of back side axial strain.

C. Prebuckling displacements around cutouts

Measured prebuckling displacements at the vertical edges of the large cutouts are presented and discussed in this section. Two displacement transducers, shown in Fig. 4, are mounted inside of the shell on magnetic bases affixed to the lower platen, and used to record the radial displacements at the center of each vertical edge of the cutouts during load application. These displacement transducers are installed on the right and left sides of the large cutout at the 3 and 9 o'clock positions, respectively. To be consistent with the strain gage rosette locations presented in Fig. 8, these respective locations are also designated RL 8 and 10. The measured radial displacements for Shell A are plotted against the applied axial load in Fig. 13, with corresponding data for Shell B shown in Fig. 14. In both figures, positive values of displacement correspond to outward radial motion of the shells. The data for the transducers on the right edges of the cutouts (RL 8) are plotted as red lines, and the corresponding data from the transducers on the left edges (RL 10) are plotted with black lines.

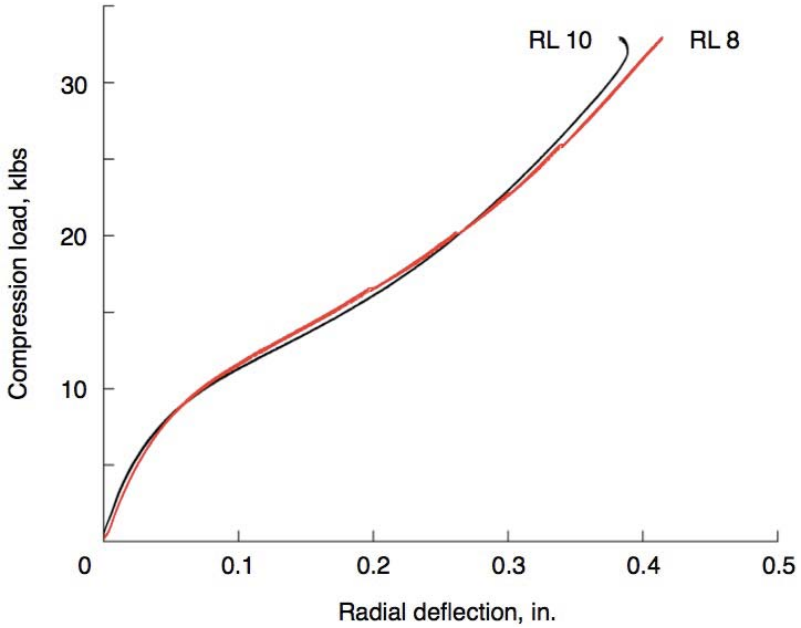

Figure 13. Shell A axial load plotted as a function of cutout radial displacements.

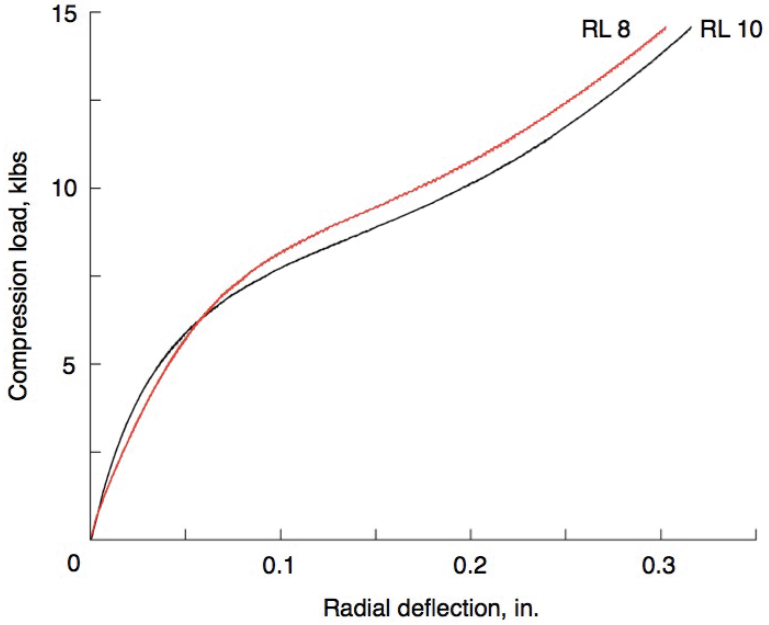

Figure 14. Shell B axial load plotted as a function of cutout radial displacements.

These measured displacements at the edges of the large cutout shown in Figs. 13 and 14 are nonlinear throughout the range of applied loading for both shells, and are also highly symmetric across the cutout width. In both cases, the maximum displacements achieved just prior to global buckling are equal to approximately 8 to 10 times the nominal 0.040-in. wall thickness of the shell sides, which is also indicative of the degree of nonlinearity in the structural response there.

D. Prebuckling strains around large cutouts

In this section, selected measurements synthesized from the 48 strain gages installed around the large cutout are plotted against the axial load from the shell compression tests. When facing the cutout as shown in Figs. 4 and 8, 24 back-to-back strain gage rosettes were located at the 12 integer clock positions around the cutout perimeter. The 8 biaxial rosettes at the 12, 3, 6 and 9 o'clock positions were designated as RL 7, 8, 9, and 10 in Fig. 8, and each rosette had 2 orthogonal strain gages. Eight of the remaining rosettes were uniaxial, and the other eight rosettes were triaxial to also measure the local shear strains. For both shells, the strains at these locations are generally symmetric across the length and width of the cutouts, and are also nonlinear with increasing load. Differences between the outside and inside strains at the same rosette location indicate that local shell wall bending was occurring around the cutout perimeter.

Measured axial strains at longitudinal (RL 7 and 9) and transverse (RL 8 and 10) locations around the large cutout are plotted against the axial load for Shell A in Fig. 15, and for Shell B in Fig. 16. Taking advantage of the high degree of symmetry in the data, each strain trace plotted here is presented as the average of either the outside or inside surface strains along the specified axes. The averaged axial strains at the locations along the shell longitudinal axis are nearly equal and opposite, indicating the presence of local shell wall bending with minimal associated membrane strain, defined as the average of the outer and inner surface strains.

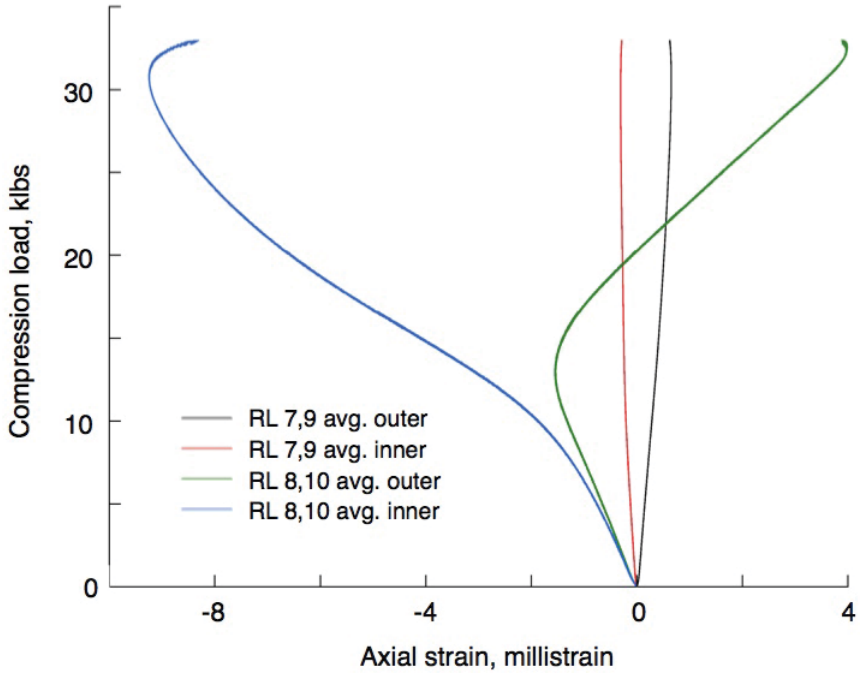

Figure 15. Shell A axial load plotted as a function of cutout axial strain.

The averaged axial strains plotted at the transverse locations on either side of the cutout diverge relatively slowly at lower applied loads, and then rapidly after about 10 klbs axial load for Shell A, and 7 klbs for Shell B. This behavior is suggestive of local buckling occurring at the cutout edge. However, no associated noises or abrupt changes in the radial displacements are observed at these loads during the tests. Qualitatively, the axial membrane strain at these locations is compressive, which corresponds to the overall applied compressive axial strain state of the shells.

The circumferential strain data at these same rosette locations are then plotted in Figs. 17 and 18 for Shells A and B, respectively. As described for Figs. 15 and 16, the outside and inside surface circumferential strains across the cutout are averaged separately before being plotted. The averaged circumferential strains shown in these figures

show similar trends to the results described above for the axial data. However, local rotations are oriented in opposite directions, so that Figs. 15 and 17, and Figs. 16 and 18, are qualitative mirror images of each other. The membrane circumferential strains at RL 8 and 10 on the cutout vertical edges are approximately equal to the magnitudes of the membrane axial strains there. The tensile circumferential membrane strains indicate that the shell expands radially under the compressive loading.

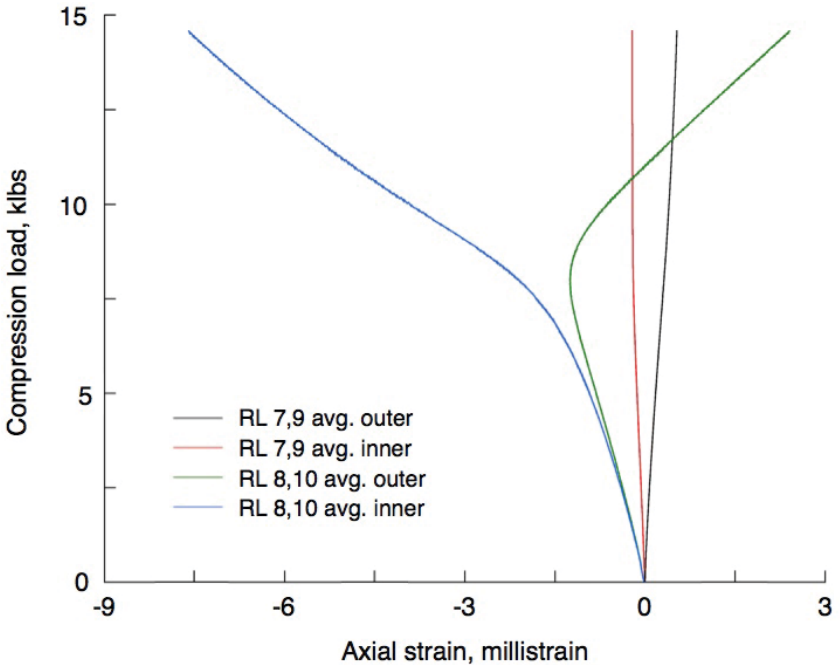

Figure 16. Shell B axial load plotted as a function of cutout axial strain.

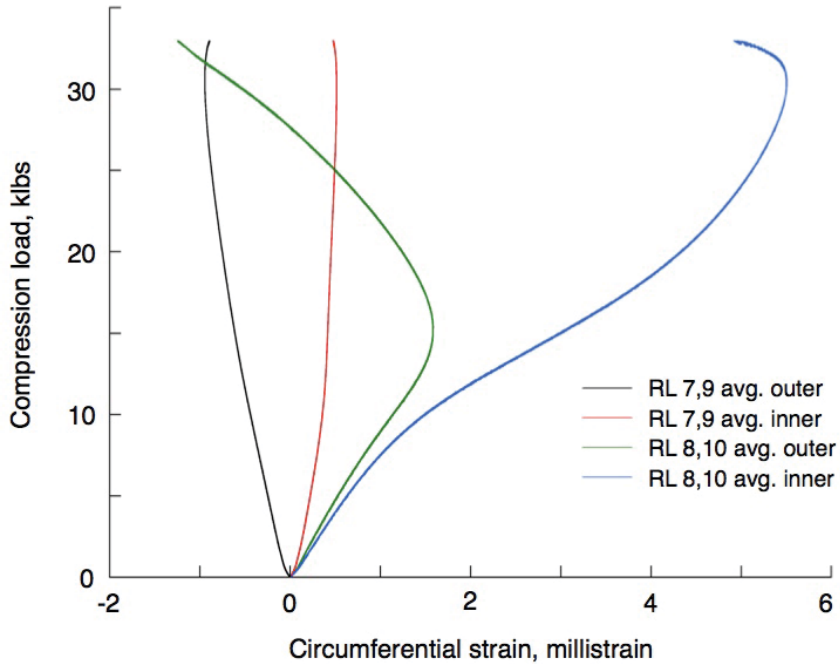

Figure 17. Shell A axial load plotted as a function of cutout circumferential strain.

E. Full-field displacement measurements

Measured full-field radial displacements, taken immediately prior to, and immediately after, global buckling, are presented and discussed in this section. Reference images for these analyses were taken before the test at zero

applied load. Separate DIC systems used to collect this imagery were positioned to view both the shell crown and the side containing the large cutout during the compression tests. Color contour plots of the radial displacements along both shell crowns are shown in Figs. 19 and 20, and corresponding plots for the shell sides with the cutouts are shown in Figs. 21 and 22. The "0" notation on the qualitative central scale and adjacent contour plot designates the color that corresponds to zero radial displacement in that plot.

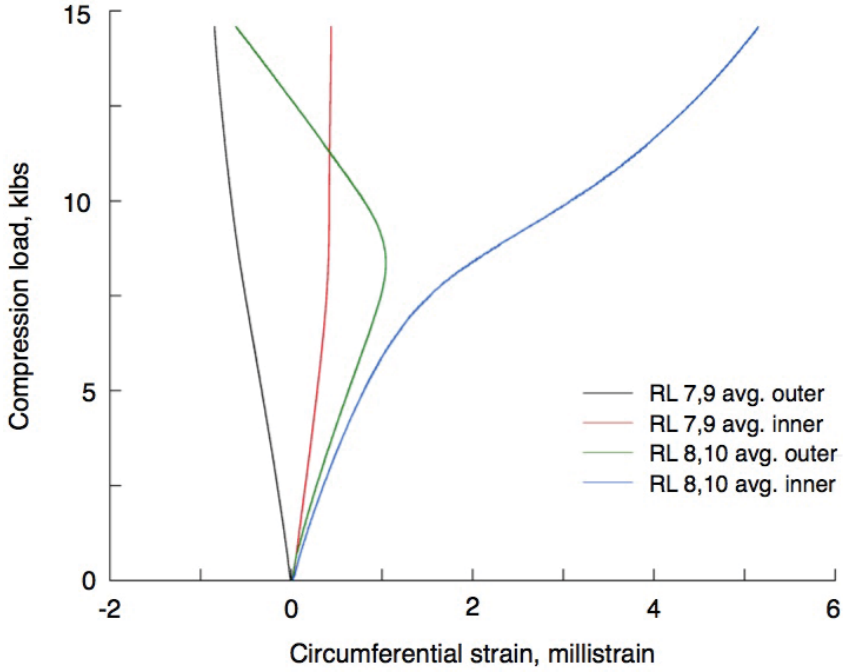

Figure 18. Shell B axial load plotted as a function of cutout circumferential strain.

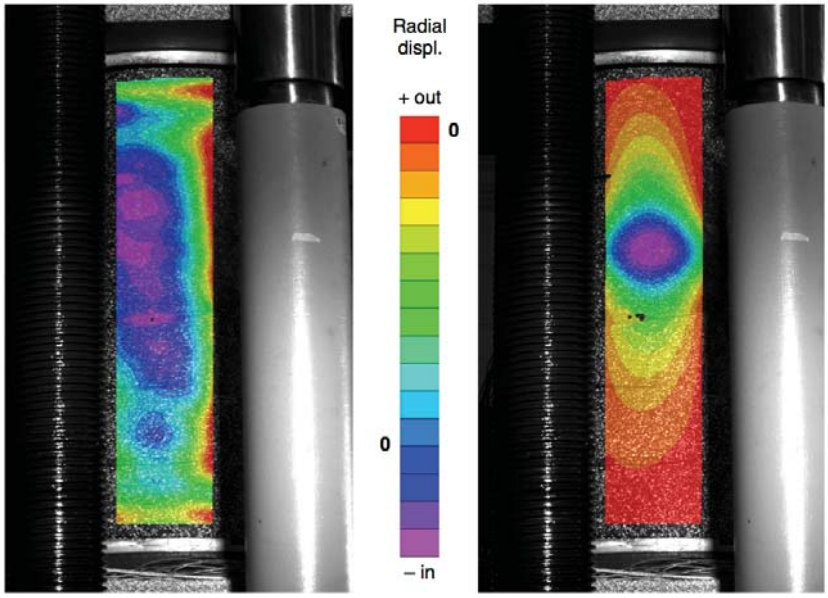

a) Buckling load = 33.0 klbs b) Postbuckling load = 20.4 klbs

Figure 19. Shell A crown measured radial displacements.

The image of the Shell A crown in Fig. 19a, acquired just prior to global buckling, shows a depressed region located on the shell crown, with several shallow ridges oriented transverse to the shell longitudinal axis. For reference, the cutout is to the right in these figures. The same image taken immediately after buckling, shown in Fig.

19b, shows a deep central depression that is generally consistent with the results observed in Ref. 10 for the pristine Shell A without the cutout. The corresponding images for Shell B show more pronounced axial waves clearly visible in the prebuckled image in Fig. 20a, and a single depression in the postbuckled image in Fig. 20b. These results are also consistent with the results presented in Ref. 10 for the pristine Shell B without a cutout.

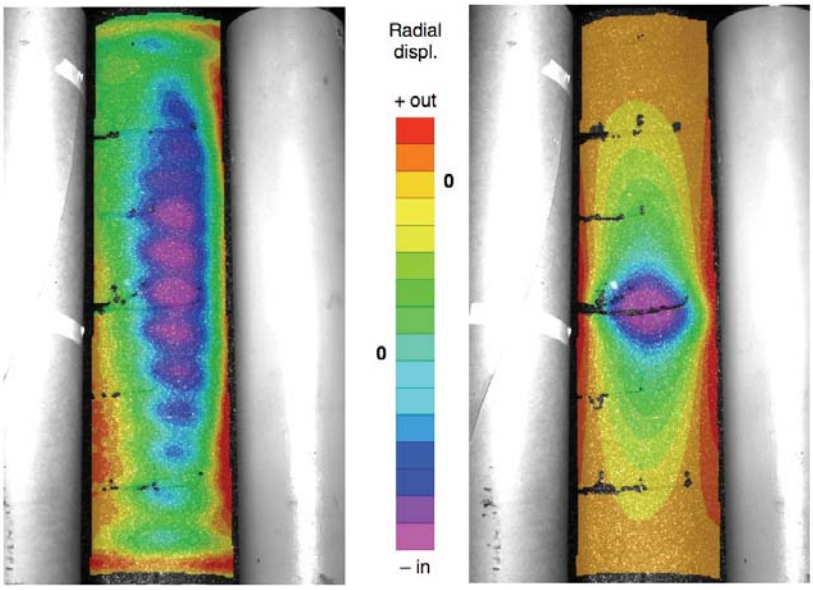

a) Buckling load = 14.6 klbs b) Postbuckling load = 11.5 klbs

Figure 20. Shell B crown measured radial displacements.

Qualitative deformations for the side of Shell A containing the cutout, taken just before and after global buckling, are shown in Figs. 21a and 21b, respectively (the black regions contained strain gage wiring, and were digitally cropped). The corresponding results for Shell B are shown in Figs. 22a and 22b. The prebuckling radial displacements in Figs. 21a and 22a at the 12 and 6 o'clock positions around the cutout perimeter were directed inwards in a semi-circular shape, and correspond to the strain states at RL 7 and 9 described in Figs. 15 to 18. The prebuckling radial displacements at the 3 and 9 o'clock positions (RL 8 and 10) were also semi-circular, but were oriented radially outwards at the cutout perimeter.

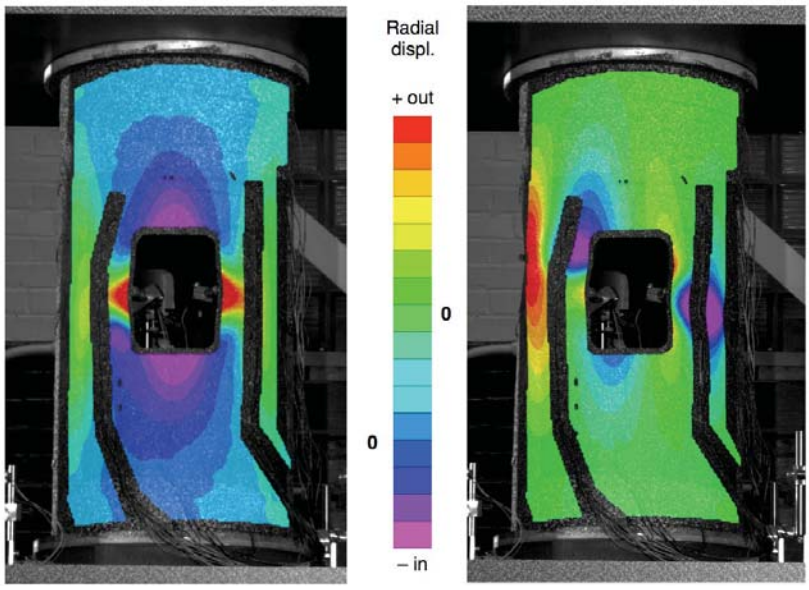

a) Buckling load = 33.0 klbs b) Postbuckling load = 20.4 klbs

Figure 21. Shell A cutout side measured radial displacements.

The qualitative displacement patterns on the shell sides containing the cutouts are shown after global buckling in Figures 21b and 22b for Shells A and B, respectively. A raised longitudinal ridge is visible in both figures to the left of the large cutout, and is also visible to the right of the cutout in Figure 20b. After buckling, inward dimples formed around the cutouts. Shell A has dimples form near the 3 o'clock, and between the 10 and 11 o'clock, positions, while the dimples for Shell B are located near the 7 and 12 o'clock positions. The cutout wall for Shell A bulges out slightly at the 2 o'clock position, while larger outward bulges are located at the 3 and 9 o'clock positions on Shell B.

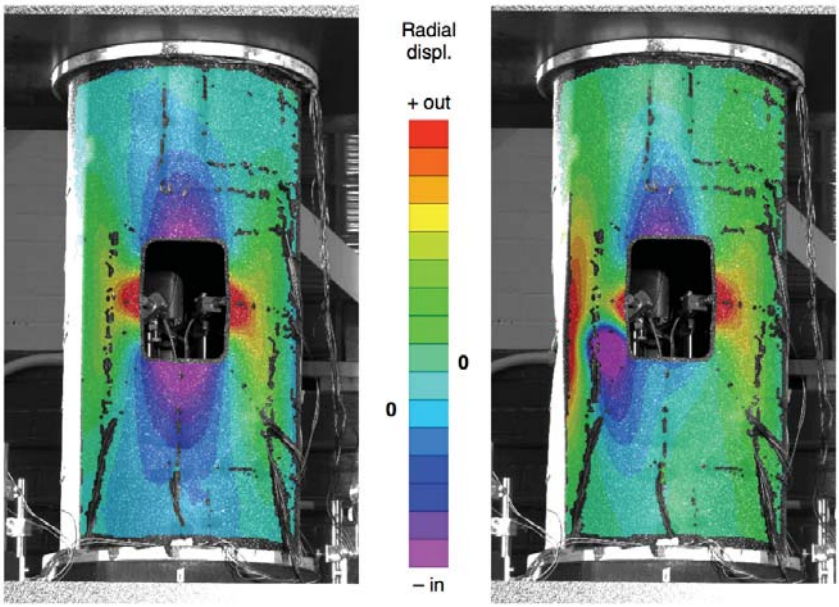

a) Buckling load = 14.6 klbs b) Postbuckling load = 11.5 klbs

Figure 22. Shell B cutout side measured radial displacements.

V. Shell structural analyses

A. Finite element models

The structural models of the tow-steered shells with and without overlaps developed previously[10, 11] were modified to include the large cutouts, as shown in Fig. 23. The assumed laminate thicknesses for the Shell A finite element model in Fig. 23a range from 16 plies (red) on the shell crown and keel, to 8 plies (blue) on the sides. In comparison, the laminate thicknesses for the Shell B finite element model were assumed to be a constant eight plies, and are not shown here. The fiber orientation angles assumed for the first tow-steered ply (ply 3) in both models are shown in Fig. 23b, and range from 45 degrees (red) on the shell sides, to 10 degrees (blue) on both the shell crown and keel.

The mesh density in the region surrounding the cutout, outlined in white in Fig. 23, was increased to better model the local structural response. A convergence study was first performed to determine the appropriate level of mesh refinement, and the results implemented on the models used for this study. The thickness-adjusted ply principal stiffness E_1 = 19.48 Mlb/in^2 of the IM7/8552 material developed in Ref. 11 was again used for the present analyses. Results of the linear finite element analyses performed for the shells with small cutouts in Ref. 11 correlated well with the measured shell prebuckling axial stiffnesses, and were much closer than the previous results for the pristine shells reported in in Ref. 10.

B. Structural analyses and results

Preliminary linear structural analyses of the shells with large cutouts were performed with the NASTRAN[15] finite element code using the models described in the previous section. Simulated end compression loads were applied to the models to predict the axial stiffness and bifurcation buckling load of the shells, and the results of these analyses are presented and discussed in this section. The predicted prebuckling axial stiffnesses listed in Table 2 compared very well with the measured data from Table 1. Although both analytical values are slightly lower than the corresponding test results, they are still within an average of 0.25 percent of the experimental stiffnesses.

For both shells, the lowest bifurcation buckling mode predicted from the shell structural analyses had a single axial half-wave, localized to the vertical edges of the cutout, that was directed radially outwards. This local buckling mode shape is shown in Fig. 24, with the corresponding predicted buckling loads listed in Table 2. However, these predictions of discrete local buckling events did not match the actual shell response observed during the tests, where the deformations around the cutout perimeter were highly nonlinear from the initiation of loading up to global buckling. In addition, the bifurcation buckling analyses predicted the existence of numerous additional local buckling modes having combinations of symmetric or asymmetric, multiple half-waves around the cutout perimeter. None of the deformations observed during the shell tests confirmed the existence of these other predicted local modes.

Table 2. Predicted performance for shells with large cutouts

Shell performance metric	Shell A	Shell B
Prebuckling axial stiffness, klb/in.	487.8	294.7
Lowest local buckling load, klbs	14.9	7.8
Lowest global buckling load, klbs	36.5	14.6

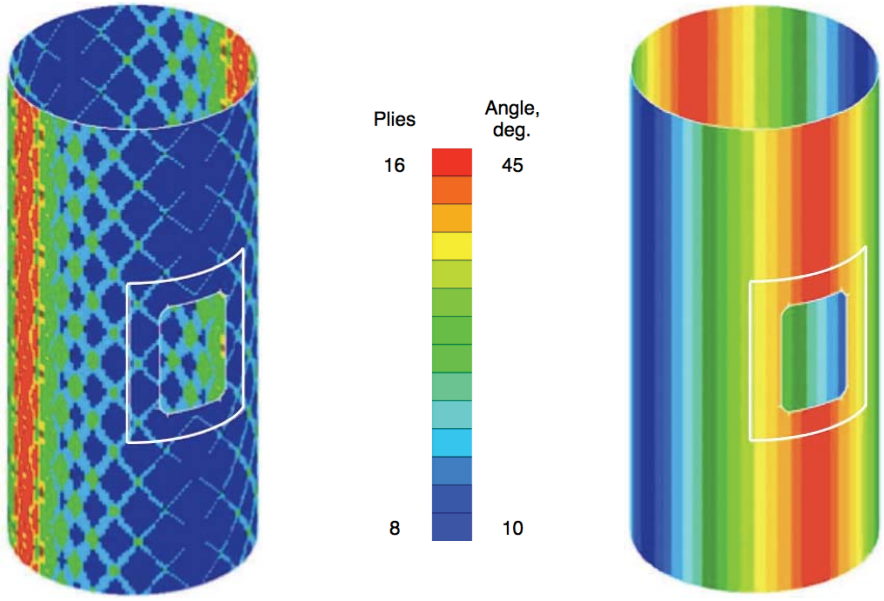

a) Shell A laminate thicknesses b) Ply 3 fiber orientation angles

Figure 23. Finite element model of tow-steered shell with large cutout.

The lowest global bifurcation buckling modes for the tow-steered composite shells were predicted to occur at 36.5 klbs and 14.6 klbs for Shells A and B, respectively, as shown in Table 2. These global modes were mode numbers 13 and 9 for Shells A and B, respectively. The predicted global buckling load for Shell A was approximately 11 percent greater than the measured shell buckling load of 33.0 klbs listed in Table 1, while the predicted global buckling load for Shell B was equal to its corresponding test value of 14.6 klbs. The corresponding analytical mode shapes are shown in Fig. 25, and have a single circumferential half-wave and numerous axial waves located simultaneously on the shell crown and keel. The computed mode shape for Shell A has approximately 18 axial half-waves with much longer wavelengths than the approximately 21 half-waves predicted for Shell B. The DIC deformations observed for Shell B before buckling show better qualitative agreement with these predicted mode shapes than the corresponding results for Shell A, which may result from the DIC speckle size, data scaling, or the ability of the DIC to track relatively small deformations.

VI. Concluding remarks

Two advanced composite tow-steered shells with large cutouts were evaluated in this study. These shells were previously tested both without cutouts and with small cutouts. Experimental methods and linear finite element

analyses were used to characterize the structural performance of the shells under end compression loads. The shells with the large cutouts had measured prebuckling axial stiffnesses and global buckling loads that were an average of 91 and 85 percent, respectively, of the corresponding values the pristine shells without cutouts.

One purpose of this investigation was to gather useful information that can help to validate existing finite element analysis tools and methods. The differences noted between the experimental buckling predictions and the linear finite element analyses indicate that more detailed geometrically nonlinear structural analyses should be performed to achieve better correlation with the actual structural response of these shells.

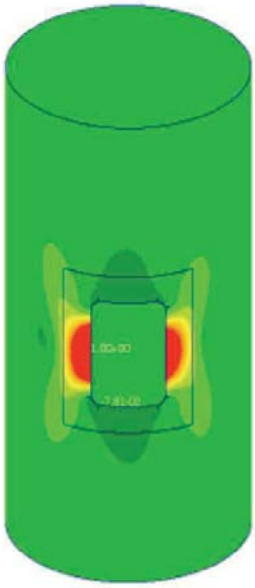

Figure 24. Predicted lowest local buckling mode shape.

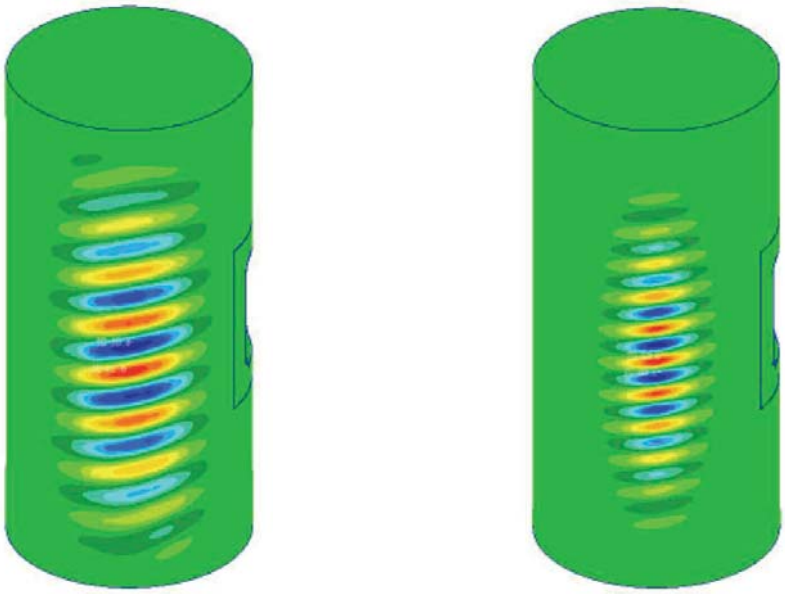

a) Shell A b) Shell B

Figure 25. Predicted lowest global buckling mode shapes.

While the tow-steered fiber orientation angles of these composite shells were not originally designed with cutouts in mind,[8] the results presented in this study and in Ref. 11 indicate that these shells with both small and large cutouts can carry a significant portion of their pristine buckling loads (i.e., without cutouts) before buckling elastically. The relatively small reductions in buckling loads and axial stiffnesses observed during these tests, and

verified using linear analyses, demonstrate the potential for using tow steering to mitigate some of the adverse effects of such design features on the overall performance of aerospace structures.

Based on the observations made in this study, designs that make more aggressive use of tow steering, and also include the cutout geometry earlier in the structural design process, may result in additional weight savings and structural performance improvements for similar shells. When the results presented in this report are used in conjunction with other studies on structural design, analysis and optimization, they may help to define tow-steered composite configurations that can help to mitigate the detrimental effects of cutouts on structural performance.

References

[1] Nemeth, M. P., and Starnes, J. H., Jr., "The NASA Monographs on Shell Stability Design Recommendations: A Review and Suggested Improvements," NASA/TP-1998-206290, 1998.

[2] Hilburger, M. W., and Starnes, J. H., Jr., "Buckling Behavior of Compression-Loaded Composite Cylindrical Shells with Reinforced Cutouts," *International Journal of Nonlinear Mechanics*, Vol. 43 (2005), pp. 1005–1021.

[3] Jegley, D. C., Tatting, B. F., and Gürdal, Z., "Optimization of Elastically Tailored Tow-Placed Plates with Holes," *Proceedings of the 44th AIAA/ASME/ASCE/AHS/ASC Structures, Structural Dynamics and Materials Conference*, Norfolk, Virginia, April 7-10, 2003, paper no. AIAA 2003-1420.

[4] Jegley, D. C., Tatting, B. F., and Gürdal, Z., "Tow-Steered Panels with Holes Subjected to Compression or Shear Loading," *Proceedings of the 46th AIAA/ASME/ASCE/AHS/ASC Structures, Structural Dynamics and Materials Conference*, Austin, Texas, April 18-21, 2005, paper no. AIAA 2005-2081.

[5] Wu, K. C., "Advanced Tow-Steered Composites Technology Development," *Proceedings of the NASA Fundamental Aeronautics Program 2012 Technical Conference*. Cleveland, Ohio, March 12-15, 2012.

[6] Evans, D. O., "Fiber Placement," *Handbook of Composites*, 2nd edition, edited by S. T. Peters, Chapman & Hall, London, 1998, pp. 476-487.

[7] Lukaszewicz, D. H.-J.A., Ward, C., and Potter, K. D., "The Engineering Aspects of Automated Prepreg Layup: History, Present and Future," *Composites Part B: Engineering*, Vol. 43, Issue 3 (April 2012), pp. 997–1009.

[8] Wu, K. C., "Design and Analysis of Tow-Steered Composite Shells Using Fiber Placement," *Proceedings of the ASC 23rd Annual Technical Conference*, Memphis, Tennessee, September 9-11, 2008, paper no. 125.

[9] Wu, K. C., et al., "Design and Manufacturing of Tow-Steered Composite Shells Using Fiber Placement," *Proceedings of the 50th AIAA/ASME/ASCE/AHS/ASC Structures, Structural Dynamics and Materials Conference*, Palm Springs, California, May 4-7, 2009, paper no. AIAA 2009-2700.

[10] Wu, K. C., et al., "Structural Assessment of Advanced Composite Tow-Steered Shells," *Proceedings of the 54th AIAA/ASME/ASCE/AHS/ASC Structures, Structural Dynamics and Materials Conference*, Boston, Massachusetts, April 8-11, 2013, paper no. AIAA 2013-1769.

[11] Wu, K. C., Turpin, J. D., Stanford, B. K., and Martin, R. A., "Structural Performance of Advanced Composite Tow-Steered Shells with Cutouts," *Proceedings of the AIAA 2014 Science and Technology Forum and Exposition*, National Harbor, Maryland, January 13-17, 2014, paper no. AIAA 2014-1056.

[12] Zalameda, J. N., Rajic, N., and Genest, M., "Signal to Noise Studies on Thermographic Data with Fabricated Defects for Defense Structures," *Proceedings of SPIE Thermosense XXVIII*, edited by J. J. Miles, G. R. Peacock, and K. M. Knettel, Vol. 6205, April 17-20, 2006.

[13] Anon., "787-8 Airplane Characteristics for Airport Planning, D6-58333, rev. H," October 2012, The Boeing Company, Seattle, Washington, downloaded 01 April 2013 from http://www.boeing.com/commercial/airports/acaps/787sec2.pdf.

[14] Sutton, M. A., Orteu, J. J., and Schreier, H., *Image Correlation for Shape, Motion and Deformation Measurements: Basic Concepts, Theory and Applications*. Springer, New York, 2009.

[15] Anon., *MSC Nastran 2012 Quick Reference Guide*, MSC Software Corporation, Santa Ana, California, 2011.